

## Electrically tunable benchtop microscope integrating TIE-based phase imaging and edge AI analysis

Hsieh-Fu Tsai <sup>a,b,1,\*</sup>, Soumyajit Podder <sup>a,c,1</sup>, I-Ming Chang <sup>d,a</sup>, Mao-Chang Ho <sup>a</sup>

<sup>a</sup> Department of Biomedical Engineering, Chang Gung University, No.259 Wenhua First Road, Taoyuan City, 333, Taiwan

<sup>b</sup> Department of Neurosurgery, Chang Gung Memorial Hospital, Keelung, No.222 Maijin Road, Keelung City, 204, Taiwan

<sup>c</sup> Department of Biomedical Engineering, National Cheng Kung University, No.1 University Road, Tainan City, 701, Taiwan

### ARTICLE INFO

#### Keywords:

Electrically tunable lens  
Cell segmentation  
Convolutional neural network  
Edge computing  
Electrowetting liquid lens  
Phase retrieval

### ABSTRACT

Optical microscopy is a pivotal technique for biomedical discovery, yet many high-performance instruments remain bulky and poorly suited for live-cell imaging and on-site computational analysis. This limits their accessibility and practical use in experiments requiring quantitative assessment of cellular dynamics. To address these challenges, we present a compact benchtop microscope that integrates an electrically tunable liquid lens (ETL), transport-of-intensity-equation (TIE)-based phase imaging, and edge-based artificial intelligence (AI) analysis within a single platform. A compact 2 $\times$  objective combined with an electrowetting ETL enables rapid, vibration-free axial defocus control with a measured magnification variation of  $3.3 \pm 0.2\%$  over a 5.9 mm focal range, facilitating electronic acquisition of defocused intensity images required for TIE-based phase recovery. The 20 cm-tall modular system incorporates transparent heater-based environmental control for microfluidic cell culture and supports optional dual-channel fluorescence and wide-field imaging modules. For automated analysis, the microscope is coupled to an edge AI device that performs on-device cell segmentation, classification, and tracking from in-focus bright-field images using a convolutional neural network. By combining ETL-based electronic defocus, non-interferometric phase imaging, and edge-based bright-field image analysis in a compact form factor, the system provides label-free phase visualization alongside low-latency AI-assisted analysis, offering a practical and compact personal microscopy solution for research, education, and training applications.

### 1. Introduction

Modern biological research increasingly demands real-time analysis of dynamic cellular processes, yet many microscopy systems remain limited by the temporal constraints of mechanical focusing, bulky optical architectures, and dependence on external computational resources. These limitations hinder the deployment of flexible, low-latency imaging platforms for live-cell experiments and on-site analysis. Recent advances in three enabling technologies—electrically tunable lenses (ETLs) for rapid, vibration-free axial focusing, non-interferometric phase imaging techniques based on the Transport of Intensity Equation (TIE), and edge computing for on-device data processing—offer an opportunity to address these constraints within compact microscopy systems. However, the systematic integration of these technologies into a single, self-contained benchtop platform remains largely unexplored.

Compact benchtop microscopes have substantially improved accessibility in biological imaging, with recent developments demonstrating

innovation across diverse technological approaches. The UC2 modular microscopy platform represents this trend, leveraging 3D printing to enable customizable optical configurations for bright-field and fluorescence imaging while maintaining research-grade performance [1,2]. This modular paradigm has inspired implementations ranging from educational platforms built from consumer components [3], to ultra-miniaturized systems for specialized neural monitoring [4], unconventional optical geometries [5,6], and alternative imaging modalities for cost-effective morphological analysis [7]. In parallel, the OpenFlexure microscope project has shown that fully 3D-printed, open-source designs can achieve reproducible and precise imaging through flexure-based mechanical positioning [8,9]. Despite these advances, most compact microscopes still rely on mechanical focusing mechanisms, which limit focusing speed, introduce vibration, and complicate long-term live-cell imaging.

Electrically tunable lenses have emerged as an effective solution to the limitations of mechanical focusing by enabling rapid, electronically controlled focal length modulation through electrowetting, deformable

\* Corresponding author.

E-mail address: [hftsaicgu.edu.tw](mailto:hftsaicgu.edu.tw) (H.-F. Tsai).

<sup>1</sup> Authors contributed equally.

polymer, or liquid crystal mechanisms [10,11]. Advances in materials science and encapsulation technologies have significantly improved the durability and thermal stability of ETLs, mitigating earlier issues related to fluid leakage and evaporation [12,13]. When integrated with digital control electronics, ETLs enable fast, repeatable axial scanning with sub-millimeter precision and minimal mechanical complexity, making them well suited for compact and portable imaging systems [14–16]. However, their integration with phase-sensitive imaging modalities introduces additional challenges related to magnification stability, defocus accuracy, and reconstruction robustness.

Phase imaging techniques have long been developed to provide label-free contrast for transparent biological specimens by exploiting optical phase shifts induced by refractive index and thickness variations. Classical methods such as Zernike phase contrast [17] and differential interference contrast (DIC) microscopy [18] enhance image contrast by converting phase variations or phase gradients into intensity modulations; however, they do not provide direct or quantitative measurements of optical phase. Building on these foundational concepts, modern quantitative phase imaging (QPI) techniques aim to recover physically interpretable optical phase information from intensity measurements [19,20]. Among these approaches, the transport-of-intensity equation (TIE) offers a particularly attractive non-interferometric framework, enabling phase reconstruction from intensity images acquired at multiple defocus planes without the need for interferometric optics [21,22]. Owing to its optical simplicity and compatibility with incoherent or partially coherent illumination, TIE-based phase imaging is well suited for compact microscope architectures.

Previous studies have demonstrated that, when combined with carefully designed optical configurations and reconstruction strategies, TIE-based methods can recover quantitative phase information with useful accuracy for a range of applications [23–25]. Nonetheless, many high-fidelity TIE implementations rely on relay-based optical layouts, stringent illumination control, or computationally intensive reconstruction pipelines, which limit their applicability in resource-constrained or real-time imaging environments [26,27]. In practice, compact implementations of TIE often involve trade-offs between system simplicity, reconstruction robustness, and absolute phase accuracy.

Edge computing provides a complementary pathway for enabling low-latency operation in compact microscopy systems by performing image acquisition, device control, and data analysis directly at the instrument level. By reducing reliance on external computers and data transfer, edge-based architectures can support responsive user interaction and real-time analysis workflows [28]. Recent intelligent microscopy platforms have demonstrated the feasibility of integrating machine learning-based analysis, such as cell detection and segmentation, into compact imaging systems [29,30]. However, the combined integration of ETL-based rapid focusing, non-interferometric phase imaging, and edge-native computation within a single benchtop microscope has not been systematically investigated.

In this work, we present a portable, multimodal benchtop microscope that integrates ETL-based electronic focusing, TIE-based phase imaging, edge computing, and an environmental control system within a compact, 3D-printed platform compatible with microfluidic cell culture. In the current implementation, AI-based segmentation, classification, and tracking are performed exclusively on in-focus brightfield images to ensure computational efficiency and robustness on edge hardware, while TIE-based phase imaging is used as a complementary modality for label-free visualization and quantitative validation using microsphere standards and biological cells. By experimentally characterizing the optical performance, phase reconstruction behavior, and on-device analysis capabilities of the integrated system, this work provides a practical framework for deploying phase-capable, edge-enabled microscopy in resource-limited and real-world research environments.

## 2. Materials and methods

### 2.1. Modular microscope design and fabrication

The benchtop modular microscope comprises a microscopic imaging module, an epifluorescence module, an environmental control unit, a wide-field imaging module, an edge computing computer, and a touch-screen display. The modular microscope was designed with computer-aided design (CAD) using Rhinoceros CAD software (Robert McNeel & Associates, USA) (Fig. 1 & Fig. 2). The work pieces for each module and chassis were 3D printed with Nylon 12 by selective laser sintering (SLS) (Fuse1, Formlabs, USA). The modular design made the optical arrangement flexible, expandable, compact, and cost-effective compared to conventional computer numerical control fabrication (CNC). Durable threads and optic mounts could be directly printed using SLS technology with high accuracy and precision. The tolerances of SLS-made workpieces fell around  $114 \pm 23 \mu\text{m}$  after sandblasting.

#### 2.1.1. Liquid lens for vibration-free rapid focusing

An electrowetting ETL employs a deformable optical element to electrically adjust the focal length [11,12]. One of the two most common ETL technologies utilizes two immiscible liquids and adjusts the meniscus via electrowetting, achieving a fast response time in a compact configuration with low power consumption. The other ETL technology utilizes optical liquid and elastomeric membranes. The focal length is adjusted by mechanically deforming the elastomeric polymer membrane [31,32]. Although the aperture is more prominent in the latter technology, the ETL and its electronics are relatively large, hindering the compactness of the optical setup.

First, we investigated how an electrowetting ETL affects magnification with five off-the-shelf microscope objectives. The objectives included three ultra-compact finite-conjugate 2X objectives from Edmund Optics, USA, #36-278 numerical aperture (NA)=0.15, #36-279 NA=0.10, and #36-280 NA=0.13, as well as two infinity-corrected 10X objectives from Olympus (CACHN10XIPC, NA=0.25, Evident Corporation, Japan) and Nikon (CFI Plan Fluor DLL 10X, NA=0.3, Nikon, Japan). The liquid lens (A39N0, Corning, USA) was positioned at the rear port of each objective within a custom-designed mount and measurement stand, both of which were created using CAD and 3D printing technology.

Theoretically, if the variable focus lens is placed at the back focal plane, there would be no change in magnification [33]. However, the back focal planes of the microscope objectives were often inaccessible because they were located within the objective body, and the lens design was often a proprietary secret [32,33]. Subsequently, we examined the alterations in magnification when the ETL was placed within the 2X objective (#36-280) near the final optical lens and among the optical elements of a conventional phase contrast 10X objective (CACHN10XIPC, Olympus).

The liquid lens was driven by the MAX14574 driver board or the USB-M driver board from the manufacturer's development kit, both providing 10-bit voltage resolution. The MAX14574 board was communicated to the edge computing computer through the I2C protocol using an in-house developed Python library [34].

#### 2.1.2. Modular optical design for brightfield and fluorescence imaging

The optical design of the benchtop microscope can be seen in Fig. 1b. The reconfigurable core imaging setup of the microscope was composed of a spacer, a microscopic imaging module, and an epifluorescence module, all connected through M4 screws and dovetail-like joints (Fig. 2).

First, the imaging module was designed. The 2X ultra-compact objective (#36-280, Edmund Optics, USA), with the backplate removed, was chosen as the imaging optics and installed on a set of C-mount threads on the 3D printed imaging module. The liquid lens component (LL, A39N0, Corning, USA) sat on a protruding structure in the middle of the C-mount thread, holding the LL against the final lens of the objective. A

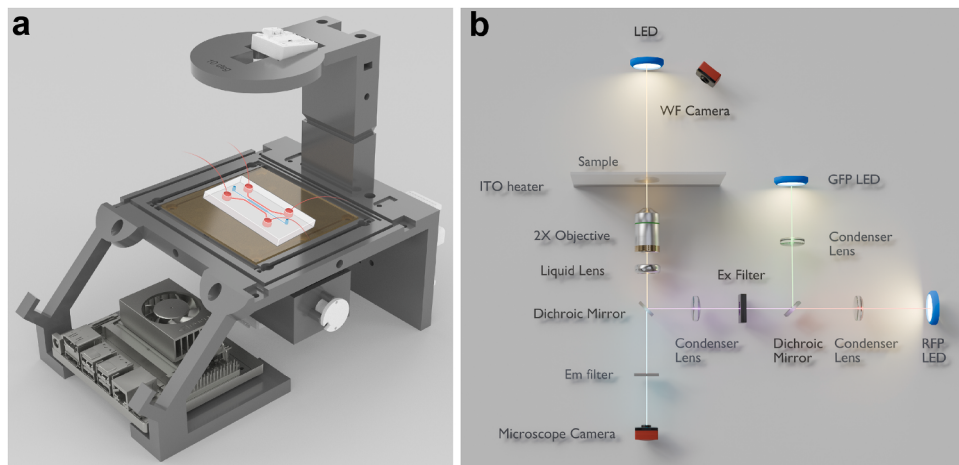


**Fig. 1.** The design of the modular benchtop microscope. (a) The CAD model of the microscope. Part of the figure was created with BioRender.com. (b) The optics setup diagram of the system. The figure utilized Blender components with permission from Ryo Mizuta Graphics.

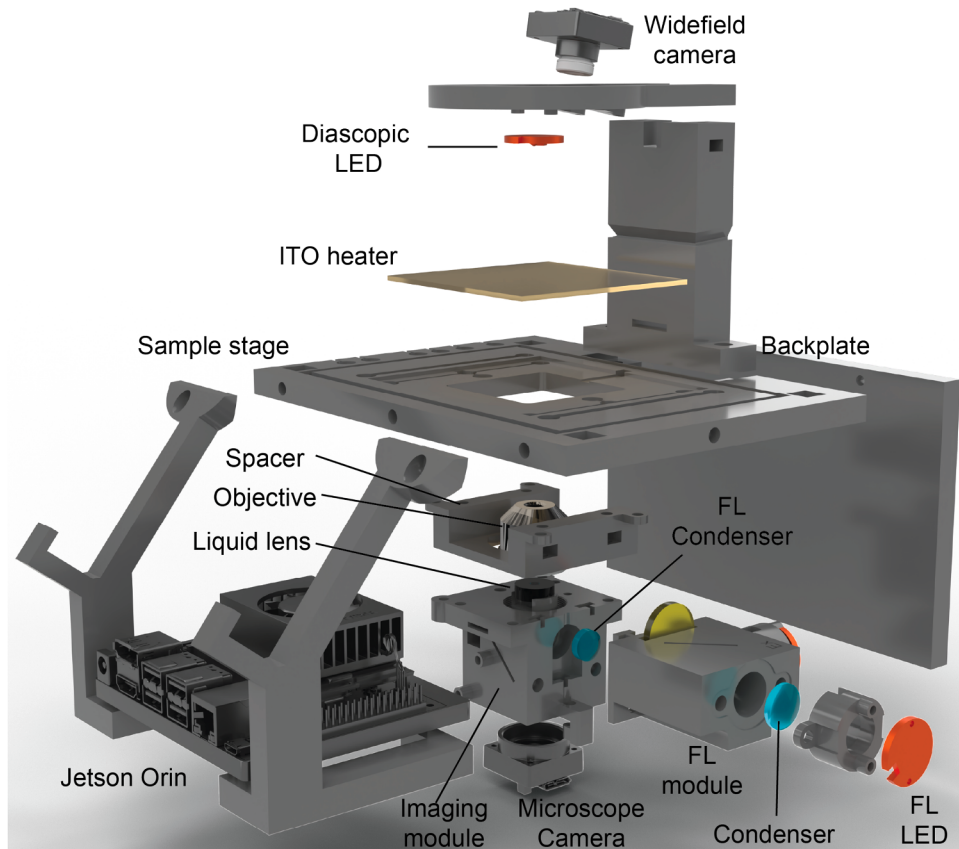


**Fig. 2.** The exploded view of the modular benchtop microscope.

dichroic mirror (59022bs, Chroma Technology Corp, USA) was inserted into a 45-degree angle slot. Slots for emission filter (EGFP/mCherry dual band, 59022m, Chroma Technology Corp, USA) insertion and camera affixation were designed at the bottom of the imaging module. An 8.3 megapixel complementary metal-oxide-semiconductor (CMOS) camera was chosen for imaging (daA3840-45uc, Basler AG, Germany). A 3 mm diameter aluminum pin was inserted into the imaging module to align and secure the dichroic mirror and the emission filter. M2.5 holes and SM05 threads were also designed and printed on the imaging module so that the MAX14574 driver board and an excitation-focusing lens (FL lens, AC127-050-A-ML, Thorlabs, USA) could be attached. The

distance from the objective mounting plane to the camera sensor was about 46.9 mm, whereas the diagonal field of view (FOV-D) of the sensor was about 1744.9  $\mu\text{m}$ . Based on the sensor diagonal (8.81 mm for a  $3840 \times 2160$  sensor with 2  $\mu\text{m}$  pixels) and the measured specimen-plane diagonal field of view (1.7449 mm), the effective system magnification is approximately 5 $\times$ . The imaging module without the dichroic mirror and fluorescence-focusing lens (FL lens) was suitable for the most straightforward compact brightfield microscope setup.

Second, an epifluorescence module could be attached to the imaging module for applications requiring two-color fluorescence. For example, fluorescence excitation for green fluorescence protein (GFP) and

red fluorescence protein (RFP) imaging could be set up to observe cells stained with dye or genetically modified with fluorescent proteins. Two monochromatic high-power light-emitting diodes (LEDs) (Thorlabs, USA) on aluminum metal-core boards, each with a center wavelength of 470 nm and 595 nm, were used. Condenser lenses were placed 8 mm from the LEDs for light collimation (72494, Edmund Optics, Singapore). A 490 nm-cutoff dichroic mirror was placed at the junction of the two LEDs, reflecting 470 nm excitation light towards the imaging module (DMLP490R, Thorlabs, USA). A multi-band excitation filter was placed next to the dichroic mirror (59022x, Chroma Technology Corp., USA). The epifluorescence module can be seen in Fig. 2.

### 2.1.3. Wide-field imaging module

An S-mount CMOS camera (daA3840-45uc, Basler AG, Germany) with a low-distortion M12 lens (M2504ZH05S, Arducam, China) was placed in the wide-field imaging module tilted at 10° to provide large-area imaging of the entire sample stage with an FOV close to 10 cm. The large FOV imaging met user needs to document experimental setups and image analysis on large samples, such as bacteria colony imaging on Petri dishes, microfluidic chip operations, and small animal motion analysis.

A 5 mm-wide chip-on-board (COB) LED strip (Adlab, Taiwan) was attached to the back pole connecting the wide-field imaging module and the sample stage. The COB LED strip provided the non-reflective illumination on the sample stage in wide-field imaging.

An LED with 625 nm center wavelength ( $625 \pm 17$  nm, Thorlabs, USA) was placed in line with the microscope objective at about 100 mm above the sample stage, providing transillumination of the sample (diascopic LED, Fig. 2). The small diascopic LED provided a partially spatially coherent light source to image transparent cells and phase imaging [35].

### 2.1.4. Measurement reference preparation

To measure the optical performance of the developed benchtop microscope, a commercial resolution target and an in-house fabricated chessboard target on a chromium mask were used (R1L3S5P, Thorlabs, USA). Fiji ImageJ and Imatest software (Imatest LLC, USA) were used to characterize the optical performance in each optical configuration, such as diagonal field of view (FOV-D), modulation transfer function (MTF), distortion, and sharpness [36,37].

To evaluate the focusing range of different objectives combined with the liquid lens, a volumetric reticle was made in-house using femtosecond two-photon laser direct writing on a piece of 5 mm-thick fused silica (LightFab 3D printer, LightFab GmbH, Germany) (Supplementary Figure S4). Specifically, markers were designed in a staircase arrangement along the z-axis every 100  $\mu\text{m}$  using the Grasshopper plugin in Rhinoceros CAD software. The laser-modified structures were visible in brightfield microscopy without any post-processing.

To validate thickness measurements obtained from TIE-based phase imaging, polystyrene (PS) microspheres with nominal diameters of 5  $\mu\text{m}$  and 10  $\mu\text{m}$  (FD230G and FH2171G, Rigor Science, China) were used as calibration standards for size uniformity and traceability. High precision thin coverglasses (No.1.5H, Marienfeld, Germany) were used as substrates for bead deposition. To enhance surface reactivity and bead adhesion, the slides were treated with oxygen plasma (PDC-001, Harrick Plasma, USA) for 2 minutes and subsequently functionalized with an amine-rich surface. Specifically, a 1% (v/v) (3-Aminopropyl)triethoxysilane (APTES) solution was prepared in 99.5% ethanol (Sigma-Aldrich, USA), and slides were incubated for 5 minutes before thorough ethanol rinsing. For bead preparation, 0.5  $\mu\text{L}$   $1 \times 10^{12}$  beads/mL suspension was diluted with 2  $\mu\text{L}$  deionized water and 1  $\mu\text{L}$  of the mixture was dispensed on the coverglass and air dried.

In addition to polystyrene microspheres, SPHERO Multiple-Fluorophore beads (FP-5066-2, Spherotech, USA) were utilized as test targets to validate thickness measurements derived via TIE. The preparation method was the same as previously described. Fluorescent beads labeled with Nile Red and Blue dyes, with a mean diameter of 5.96  $\mu\text{m}$ ,

served as reference standards during these tests. Thickness reference measurements were performed both in air and in water as dispersion media to evaluate consistency and accuracy under varying conditions.

### 2.1.5. Environmental control

A piece of transparent heating glass (indium tin oxide glass, ITO glass, 85 × 95 × 1.8 mm [L×W×H], 7 Ω, Rui long Corporation, Taiwan) provided the temperature required for cell survival on the sample stage. Double-lead copper foil tapes were affixed to both sides of the ITO glass, serving as bus electrodes (Teraoka Seisakusho Co. Ltd., Japan). High-current pogo pins (F360C, TESPRO, Japan) and in-house-made conductive copper washers were screwed into the designed slots on the sample stage, conducting the electrical current for Joule heating of the ITO glass. The non-conductive Nylon 12 sample stage provided the necessary electrical insulation. A high-precision temperature controller (TEC-1161, Meerstetter Engineering, Switzerland) with a K-type thermocouple (Tecpel, Taiwan) was used to control the heating of the ITO heater.

### 2.1.6. Edge computing computer as the integrated controller

An edge computing single-board computer, the NVIDIA Jetson Orin NX development kit (Waveshare, China) with 16GB RAM, was integrated in the benchtop microscope as the operating computational platform for the control of the LEDs, voltage driving of the liquid lens, image acquisition, environmental control, and image processing. A graphical user interface (GUI) using the PyQt library was built in-house to control the compact microscope (Supplementary Figure S10). An optional liquid crystal display (LCD) touchscreen (13", Waveshare, China) was connected as the human-machine interface. The system can also be controlled remotely via a wireless internet connection. The Jetson Orin edge computer enables 100 tera-operations per second at INT8 (TOPs) on a 1024-core graphical processing unit (GPU) with 32 tensor cores at 918MHz. GPU acceleration enables machine learning and computer vision applications, which can increase microscopy data processing accuracy and throughput [38–40].

The GUI enables dual-channel fluorescence excitation (565 nm for RFP and 488 nm for GFP via modular LED drivers), precise electrowetting liquid lens actuation through dual sliders (coarse adjustment: 0–1023 arbitrary units in discrete steps of 10 a.u. via a 10-bit DAC output to the MAX14574 driver board; fine adjustment: incremental steps of 1 a.u.), dynamic camera exposure control, and closed-loop temperature regulation of the transparent ITO stage heater (maintained at 37 °C via PID control). The interface supports acquisition of in-focus and electronically defocused image stacks required for TIE-based phase reconstruction, as well as independent execution of on-device You Only Look Once version 8 (YOLOv8) instance segmentation and classification on in-focus bright-field images [41]. All hardware components, including the CMOS camera, liquid lens driver, excitation LEDs, and environmental sensors, are interfaced directly with the Jetson Orin NX, enabling fully integrated, standalone operation with GPU-accelerated processing for edge AI analysis.

## 2.2. Cell culture and maintenance

Mouse brain endothelial cells (bEnd.3), rat aortic smooth muscle cells (A-10), and human monocytes (THP-1) were acquired from the Bioresource Collection and Research Center (BCRC, Taiwan) and cultured according to recommended protocols. Specifically, bEnd.3 and A-10 cells were grown in Dulbecco's Modified Eagle Medium (DMEM) supplemented with 10% Fetal Bovine Serum (FBS) and 1X antibiotics/antimycotics mix, while THP-1 cells were cultured in Roswell Park Memorial Institute 1640 medium (RPMI 1640) with 10% FBS and 0.05 mM 2-mercaptoethanol. All reagents were acquired from Thermo Fisher Scientific unless otherwise noted. Cells were grown at 37 °C in a humidified environment with 5% CO<sub>2</sub> (Forma 310, Thermo Fisher Scientific, USA). Cells were passaged every two days or when they reached 80% confluence using the TrypLE enzyme (ThermoFisher Scientific, USA).

Cells were preserved in Cellbanker cryopreservation solution (Zenogen, Japan) and stored in the aqueous phase of liquid nitrogen.

### 2.3. Phase recovery using the transport-of-Intensity equation

The transport-of-intensity equation (TIE) provides a deterministic, non-interferometric framework for phase retrieval by relating axial intensity variations to transverse phase gradients under the paraxial approximation. The theoretical foundation of TIE was established by Teague, who showed that the phase  $\phi(x, y)$  and intensity  $I(x, y, z)$  of a scalar optical field satisfy a continuity-like equation derived from energy conservation during free-space propagation [21]. This formulation enables phase recovery from intensity-only measurements acquired at multiple defocus planes and has since become a cornerstone of label-free phase microscopy.

In practice, TIE inversion is affected by noise, partial coherence, and boundary conditions. Guigay et al. analyzed the validity and limitations of TIE-based phase retrieval in the Fresnel regime, emphasizing the importance of stable axial intensity derivatives and appropriate defocus distances for accurate reconstruction [42]. Gureyev et al. further clarified the solvability conditions of the TIE and demonstrated robust Fourier-domain Poisson solvers under periodic boundary assumptions [43]. Building on these theoretical developments, Zuo et al. demonstrated high-speed TIE phase imaging by integrating an electrically tunable lens (ETL) into a relay-based microscope, enabling rapid electronic refocusing at constant magnification [44].

In the present work, an electrowetting-based electrically tunable lens was integrated into a compact, relay-free microscope architecture to enable fast, vibration-free axial scanning without mechanical motion. Compared with relay-based ETL configurations, the relay-free design provides increased flexibility in selecting defocus distances, allowing adaptation to samples with varying thicknesses and phase gradients. For TIE-based phase reconstruction, three intensity images were acquired at the in-focus, under-focus, and over-focus planes.

Illumination was provided by a partially coherent LED source with a central wavelength of  $\lambda = 625$  nm and an emitting area of approximately  $1 \times 1 \text{ mm}^2$ , positioned about 100 mm from the sample plane without condenser optics. This configuration yielded an estimated illumination numerical aperture of  $NA_{\text{illum}} \approx 0.005$ . With the numerical aperture of the  $2\times$  objective given by  $NA_{\text{obj}} = 0.13$ , the resulting coherence parameter  $S = NA_{\text{illum}}/NA_{\text{obj}} \approx 0.04$ , placing the system within a quasi-coherent regime in which the TIE approximation is commonly applied for the defocus distances employed.

The axial intensity derivative was estimated using a central finite-difference approximation from the under-focus ( $I_-$ ) and over-focus ( $I_+$ ) images,

$$\frac{\partial I}{\partial z} \approx \frac{I_+ - I_-}{2\Delta z}. \quad (1)$$

The TIE source term was defined as

$$J = -k \frac{\partial I}{\partial z}, \quad (2)$$

where  $k = 2\pi/\lambda$ .

Phase recovery was implemented using a two-stage FFT-based regularized Poisson inversion following Teague's auxiliary-function formalism [21]. An intermediate scalar potential  $\psi$  was first reconstructed by solving a Poisson equation driven by the source term  $J$ . Rather than explicitly constructing the auxiliary field in real space, the solution was obtained implicitly in the Fourier domain. Let  $U$  and  $V$  denote the spatial frequency coordinates in the horizontal and vertical directions, respectively, and define the Fourier-domain differential operators

$$C_x = 2j\pi U, \quad C_y = 2j\pi V. \quad (3)$$

The Fourier-domain solution of the regularized Poisson equation was expressed as

$$\mathcal{F}\{\psi\} = \frac{\mathcal{F}\{J\}(C_x^2 + C_y^2)}{\alpha + (C_x^2 + C_y^2)^2}, \quad (4)$$

where  $\alpha$  is a scalar regularization parameter. This stabilized inverse Laplacian with biharmonic regularization suppresses low-frequency noise amplification and improves numerical robustness under weak or noisy intensity gradients.

Spatial phase gradients were subsequently computed as

$$\frac{\partial \phi}{\partial x} = \frac{\partial \psi / \partial x}{I_0}, \quad \frac{\partial \phi}{\partial y} = \frac{\partial \psi / \partial y}{I_0}, \quad (5)$$

where  $I_0$  denotes the in-focus intensity image. In the second stage, the recovered phase gradients were integrated by solving a second regularized Poisson equation to obtain the final phase map  $\phi_{\text{retrieved}}$ .

All Poisson equations were solved in the Fourier domain using fast Fourier transforms, which implicitly impose periodic boundary conditions [43]. To mitigate boundary-induced artifacts, quantitative analysis was restricted to the central region of the reconstructed phase maps. The regularization parameter was fixed at  $\alpha = 1 \times 10^{-4}$ , selected empirically based on background noise levels estimated from object-free regions.

To further suppress high-frequency noise, Gaussian smoothing with a standard deviation of  $\sigma = 4$  pixels was applied to the recovered phase maps prior to quantitative analysis. Optical path length (OPL) and apparent sample thickness were subsequently computed from the retrieved phase according to

$$\text{OPL} = \frac{\lambda \phi_{\text{retrieved}}}{2\pi}, \quad t_{\text{apparent}} = \frac{\lambda \phi_{\text{retrieved}}}{2\pi(n_1 - n_0)}, \quad (6)$$

where  $n_1$  and  $n_0$  denote the refractive indices of the sample and surrounding medium, respectively.

For thickness estimation from the recovered phase, knowledge of the refractive indices of the imaged samples and their surrounding media is required. In this study, polystyrene (PS) microbeads with a refractive index of 1.59 reported by manufacturer were used as calibration objects, immersed in air (refractive index of 1.00) or deionized water (refractive index of 1.33), enabling direct conversion of phase to physical thickness. For biological cells, where refractive indices are not precisely known and may vary spatially, thickness values are interpreted as apparent (optical-path-equivalent) thicknesses under assumed relative refractive indexes. Specifically, the refractive index of bEnd.3 cells remains uncharacterized; therefore, a refractive index range of 1.370–1.380 reported for corneal endothelial cells was adopted as a surrogate [45]. Similarly, the refractive index of A-10 smooth muscle cells is undocumented, and the value reported for airway smooth muscle cells ( $1.360 \pm 0.004$ ) was used as a pragmatic surrogate [46]. For THP-1 cells, a refractive index of 1.375 was assumed, consistent with typical values reported for similar cell types [47]. The surrounding cell culture medium was assigned a refractive index of 1.337, corresponding to standard aqueous biological media.

### 2.4. Software architecture and AI inference pipeline

The microscope software framework is implemented entirely in Python and operates on an Ubuntu environment in NVIDIA JetPack on the Jetson Orin NX platform. The system adopts a multi-process architecture with asynchronous inter-process communication mediated by Qt signal-slot mechanisms.

At the hardware interface layer, image acquisition is performed using the Basler Pylon SDK, while peripheral devices—including the electrowetting liquid lens, excitation LEDs, and environmental sensors—are controlled through I<sup>2</sup>C and GPIO interfaces. All coordination between hardware actuation and image acquisition is achieved through software triggering. The GUI, implemented using PyQt5, functions as the central orchestration layer, providing real-time control of imaging parameters, liquid-lens focusing, fluorescence excitation, temperature regulation, and analysis execution. Detailed GUI layout and functionality are provided in Supplementary Section S3 and Fig. S10.

For AI-based image analysis, the system employs the Ultralytics YOLOv8 framework for instance segmentation [41]. In the current implementation, AI inference is intentionally performed exclusively

on in-focus bright-field images for computational efficiency and low-latency performance on edge hardware. TIE-recovered phase and thickness maps are not used as network inputs. However, individual region of interests of individual cells can be cropped according to YOLOv8's bounding box and forward for TIE-based phase imaging.

For video analysis, recorded image sequences are processed frame-by-frame using the same YOLOv8 inference pipeline. Each frame is passed to the network independently, and annotated frames are encoded into output video files for visualization and downstream tracking analysis. The architectural details of the YOLOv8m network employed for segmentation are provided in Supplementary Section S5 and Fig. S13.

## 2.5. Multiclass live-cell segmentation and tracking powered by edge computing

Building on the software architecture and AI inference pipeline described in Section 2.4, we evaluated the performance of the edge-computing microscope for multiclass live-cell segmentation and tracking in a biologically relevant microfluidic environment.

To generate training and validation datasets, a custom-designed microfluidic cell culture platform fabricated from poly(methyl methacrylate) (PMMA) was used, featuring dual channels with dimensions of  $30 \times 3 \times 0.07$  mm [L×W×H], as described in our previous work [40]. Three distinct cell types, mouse brain endothelial cells (bEnd.3), rat aortic smooth muscle cells (A-10), and human monocytes (THP-1), were cultured either independently or co-cultured. For co-culture experiments, a mixed medium with a 2:1 ratio of DMEM to RPMI 1640 was employed to maintain cell viability across cell types.

To validate segmentation results under multiclass conditions, selected cell populations were fluorescently labeled with Calcein AM prior to seeding, while other cell types remained unlabeled. Fluorescence images were used solely for validation and visualization and were not provided as inputs to the segmentation network, which operated exclusively on brightfield images. Representative examples of brightfield-based segmentation are shown in Fig. 6 and Supplementary Fig. S15.

Instance segmentation was performed using a YOLOv8-based model deployed on the Jetson Orin NX platform. The dataset comprised 180 manually annotated brightfield images, of which 150 were allocated for training and 30 for validation. The training set included 50 images per cell type, corresponding to three segmentation classes. Network training was conducted for 250 epochs using the CUDA-enabled GPU on the Jetson Orin NX, with a learning rate of 0.002 and a momentum of 0.9. Separate models were trained for single-class and multiclass segmentation tasks.

For evaluation, 10 images per cell type were used for single-class inference, and an additional 10 images were reserved for multiclass inference. Automated cell counting was integrated directly into the inference pipeline, enabling quantification of cell populations during live imaging experiments. Video-based segmentation and subsequent cell tracking results are available as Supplementary Movies S1 and S2.

To evaluate the dynamic behavior of monocytes within video datasets, the spatial coordinates were derived from YOLOv8 instance masks across sequential frames. These coordinates were subsequently processed using TrackPy [48], a robust particle-tracking library that assigns unique identifiers to individual cells and reconstructs their spatiotemporal trajectories. Tracking performance was quantitatively evaluated against manually annotated human ground-truth trajectories. In the ground truth, individual cells were identified and linked across consecutive frames by expert visual inspection, providing frame-resolved cell identities and trajectories. Automated trajectories were generated by linking YOLOv8-detected cell instances using the TrackPy library [48], with a search range of 15 pixels, memory of 5 frames to tolerate transient detection losses, and an adaptive stop threshold of 5 pixels.

Tracking performance was evaluated using metrics from the CLEAR MOT framework [40,49]. Two complementary measures were em-

ployed: Multiple Object Tracking Precision (MOTP) and Multiple Object Tracking Accuracy (MOTA).

MOTP quantifies spatial localization accuracy of matched object-track pairs and is defined as

$$\text{MOTP} = \frac{\sum_{t,i} d_{t,i}}{\sum_t c_t},$$

where  $d_{t,i}$  is the Euclidean distance between the centroid of a tracked object and its corresponding ground-truth object for match  $i$  at frame  $t$ , and  $c_t$  is the number of correctly matched object-track pairs at frame  $t$  [49].

MOTA captures configuration-level tracking performance by accounting for missed detections, identity mismatches, and false positives:

$$\text{MOTA} = 1 - \frac{\sum_t (m_t + mme_t + fp_t)}{\sum_t gt_t},$$

where  $m_t$ ,  $mme_t$ ,  $fp_t$ , and  $gt_t$  denote missed detections, identity mismatches, false positives, and ground-truth objects at frame  $t$ , respectively [49].

## 3. Results

In this investigation, an electrowetting liquid lens facilitated phase retrieval via the TIE, enabling analysis of polystyrene microspheres, bEnd.3 endothelial cells, A-10 smooth muscle cells, and THP-1 monocytes cultured in a microfluidic platform. This approach provided label-free phase-delay maps and bead-calibrated thickness estimates that support qualitative visualization and quantitative checks on calibration objects.

### 3.1. Rapid vibration-free focusing with minimal magnification change

Electronically controlled focusing was implemented using an electrowetting liquid lens to enable rapid axial defocus adjustment without mechanical translation. By modulating the applied voltage, the curvature of the liquid–liquid interface was varied, resulting in controlled shifts of the focal plane along the optical axis. This electronic focusing scheme permits acquisition of multiple axially displaced intensity images required for transport-of-intensity-equation (TIE) phase reconstruction, while avoiding mechanical motion and associated vibrations.

The liquid lens provided a continuous axial focusing range of up to 5.9 mm on the 36–280 2 $\times$  objective (Fig. 3), which is sufficient for typical live-cell imaging applications. Because the liquid lens could not be positioned exactly at the objective back focal plane, voltage-induced focusing introduced a finite change in system magnification (severe magnification change up to 97.9% were found when the liquid lens was placed on the back aperture of selected infinity-corrected objective available on the market). In comparison, for 36–280 objective, the measured magnification variation across the whole focusing range was limited to  $3.3 \pm 0.2\%$ . Within the voltage range used for cellular imaging in our microfluidic cell culture chip (256–640 arbitrary units), the magnification change was further reduced to 0.51%. The effective axial defocus increment corresponding to a single step of the fine voltage control was 6  $\mu\text{m}$ . The relationship between applied liquid-lens voltage and working distance was monotonic and linear, with a correlation coefficient of  $R^2 = 0.9984$ , as shown in Supplementary Figure S5.

Under this configuration, the effective sampling at the specimen plane is approximately 0.40–0.43  $\mu\text{m}$  per pixel, corresponding to an effective magnification of  $\sim 5\times$  on the nominal 2 $\times$  objective magnification.

Optical performance was evaluated using Imatest software with a lithographically fabricated checkerboard target under monochromatic illumination (625 nm) (Supplementary Fig. S7). Automated region-of-interest (ROI) detection was performed at both central and peripheral field locations, with representative edge analysis conducted on a selected ROI. The measured edge spread function exhibited a 10–90% intensity transition over 5.15 pixels, indicating moderate edge sharpness.

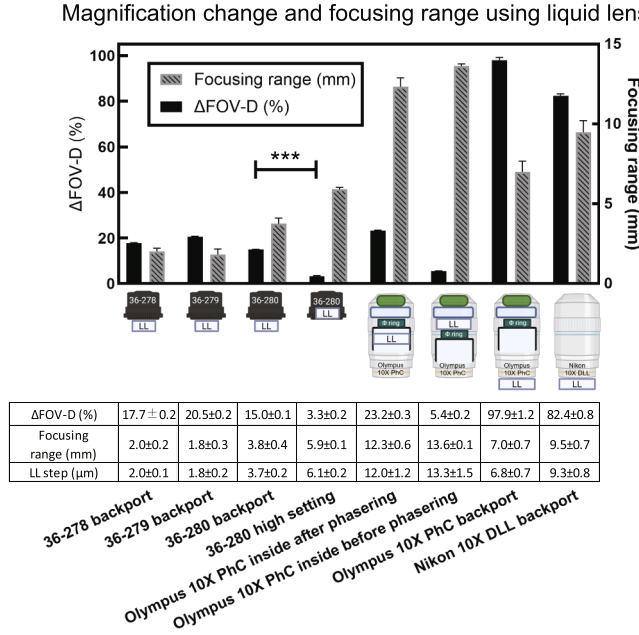


**Fig. 3.** Magnification changes and focusing range of various microscope objectives used together with a liquid lens (LL). DLL denotes the dark low low in the Nikon phase contrast objective. FOV-D denotes the diagonal field of view.

Modulation transfer function (MTF) analysis showed maximal contrast at low spatial frequencies, with a measured MTF50P of 0.080 cycles per pixel (corresponding to 97.7 lp/mm) and a gradual contrast roll-off toward higher spatial frequencies, consistent with cell-scale lateral resolution suitable for whole-cell imaging and downstream segmentation tasks.

To independently validate the frequency-domain MTF results in the spatial domain, lateral resolution was further assessed using a standardized NBS 1963A resolution target (R1L3S5P, Thorlabs, USA), as detailed in Supplementary Section S2.3. As shown in Supplementary Figures S8 and S9, line-pair elements up to 203 lp/mm (4.93 μm period) were clearly resolved exceeding the 10% Rayleigh criterion, confirming diffraction-limited performance and agreement with the MTF-predicted contrast transfer.

Geometric distortion analysis revealed slight barrel distortion under Third-Order and Arctangent models (LGD values of 1.36 and 1.31, respectively), while the Fifth-Order model exhibited increased distortion at the field periphery (LGD of -4.43). The negative SMIA TV distortion (-1.67%) indicates mild inward edge curvature, whereas the diagonal field of view (12.04°) and near-unity pixel aspect ratio (1.0018) confirm overall geometric fidelity of the imaging system. For applications requiring stringent spatial accuracy, residual distortion could be mitigated through digital correction or optical optimization.

### 3.2. Phase imaging using rapid z defocusing with liquid lens

The validity of phase imaging under electronically controlled axial defocusing was evaluated by implementing the transport-of-intensity equation (TIE) using the ETL to generate under-focus and over-focus intensity planes. Phase retrieval was performed from electronically defocused image triplets, confirming that ETL-based axial scanning preserves the phase information required for TIE reconstruction under the tested conditions.

Although liquid-lens tuning introduces a finite magnification variation across its full operating range (approximately 3.3%), the 1024-step digital control resolution results in an incremental magnification change of only ~0.0032% per step. As the defocus distances used

for TIE acquisition correspond to only two steps, the resulting magnification mismatch between defocused planes should be negligible relative to the system lateral resolution.

Fig. 4 presents representative TIE reconstruction results for a 10 μm polystyrene microbead in deionized water at a defocus distance of 12 μm. The in-focus image (Fig. 4a), reconstructed phase map (Fig. 4b), and apparent thickness map (Fig. 4c) show a peak thickness of approximately 10 μm. The three-dimensional thickness rendering (Fig. 4d) exhibits symmetric morphology, while the horizontal thickness profile (Fig. 4e) enables quantitative assessment of full width at half maximum (FWHM).

The retrieved thickness and FWHM values for microspheres of varying diameters in air and water exhibit distinct trends, as illustrated in Table 1. A defocus distance of 12 μm was used for image capture and analysis in this table. For 5 μm beads, thickness was overestimated in air ( $5.13 \pm 1.03$  μm, -2.56%) and underestimated in water ( $4.74 \pm 0.82$  μm, 5.16%). Larger 10 μm beads exhibited minimal errors, with thickness values closely matching the nominal size in air (0.56%) and slightly deviating in water (2.53%). The smaller beads (5.96 μm) demonstrated larger errors in thickness, particularly in air (10.18%), which may still arise from minute difference of refractive indexes. Thickness measurements were consistently more accurate in the air, and larger beads showed reduced relative errors compared to smaller ones. FWHM measurements exhibited an inverse trend, with deviations higher in air than in water. For 5 μm beads, errors were -9.90% in air and -12.71% in water, while for 10 μm beads, the FWHM was underestimated in air (11.83%) and closely matched in water (-0.65%). The 5.96 μm diameter beads showed moderate deviations in both media.

The SNR was calculated as the peak height above the baseline divided by the standard deviation of the baseline-corrected thickness values in regions outside the peak base. This approach follows standard practices in peak analysis for spectroscopic and chromatographic profiles, where SNR is defined as the ratio of the peak amplitude to the standard deviation of the baseline noise in signal-free regions. These results underscore the influence of bead size and medium on optical phase retrieval accuracy, with larger beads in water achieving lower relative error under the tested conditions.

For biological samples, thickness maps are reported as apparent thickness under assumed refractive indices ( $n_1 = 1.36 - 1.38$ ,  $\Delta n = 0.03 - 0.05$ ). A  $\pm 0.01$  uncertainty in  $\Delta n$  introduces an estimated 7–10% systematic error; therefore, optical phase delay (radians), which is independent of refractive-index assumptions, is reported alongside apparent thickness. The dependence of recovered microsphere thickness on defocus distance is provided in Supplementary Fig. S16. Gaussian smoothing with a kernel size of 4 pixels was applied throughout the reconstruction to suppress background noise.

Fig. 5 illustrates in-focus images, phase-retrieved TIE images, and apparent thickness under assumed refractive index (RI) images for three different cell types: endothelial cells, smooth muscle cells, and monocytes, each captured at a defocus distance of 12 μm. Original in-focus brightfield images in grayscale (panels a, d, and g) serve as baseline references, displaying the general morphology of the cells. The TIE phase-retrieved images (panels b, e, and h), measured in radians, reveal the phase variations induced by the cellular structures, emphasizing differences in the OPL across the cells. These phase images elucidate the internal cellular architecture with high precision. The corresponding retrieved thickness images (panels c, f, and i), quantified in micrometers, offer a direct measurement of cellular morphology, translating phase changes into tangible thickness values.

The images of endothelial cells (panels a-c) demonstrate detailed internal structures, with a maximum apparent thickness of approximately 10 μm, underscoring the sensitivity of the method to subtle structural variations. Smooth muscle cell images (panels d-f) exhibit a less distinct phase profile but reveal a clear thickness gradient, peaks at around 6 μm, which may be indicative of the structural composition of the cell along with the characteristic striations of this type of cell. These stri-

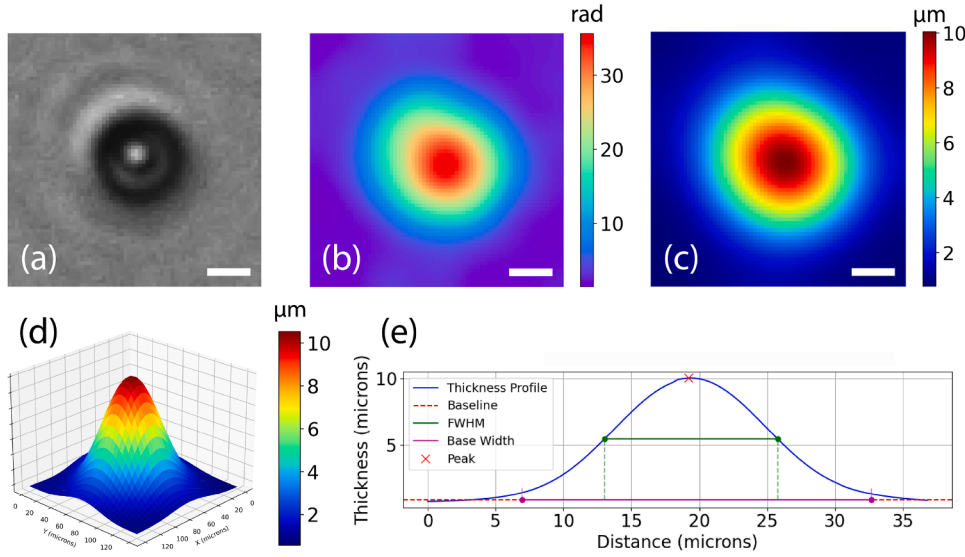


**Fig. 4.** (a) The original in-focus image, (b) the TIE phase retrieved image in radian, and (c) the thickness retrieved image in  $\mu\text{m}$  of a microbead for the defocus distance of 12  $\mu\text{m}$ . (d) The 3D thickness retrieved image of a microbead. (e) Plot of thickness vs horizontal distance along the middle of the image. Scale bars denote 5  $\mu\text{m}$ .

**Table 1**

Retrieved thickness and full width at half maximum (FWHM) (mean  $\pm$  standard error of the mean) for polystyrene (PS) microspheres of different nominal diameters imaged in air and deionized water using TIE-based phase reconstruction. Relative errors in thickness ( $\delta$ Thickness) and FWHM ( $\delta$ FWHM) are reported with respect to the nominal bead diameters. The signal-to-noise ratio (SNR) was calculated from the reconstructed thickness profiles as the ratio of peak amplitude to the standard deviation of baseline noise in signal-free regions, providing an indicator of reconstruction robustness under fixed reconstruction parameters.

Bead Size ( $\mu\text{m}$ )	Medium	Thickness ( $\mu\text{m}$ )	FWHM ( $\mu\text{m}$ )	$\delta$ Thickness (%)	$\delta$ FWHM (%)	SNR
5	Air	$5.13 \pm 1.03$	$5.49 \pm 0.68$	-2.56	-9.90	$39.2 \pm 9.4$
5	Water	$4.74 \pm 0.82$	$5.64 \pm 0.96$	5.16	-12.71	$61.5 \pm 16.7$
10	Air	$9.94 \pm 0.93$	$8.82 \pm 1.26$	0.56	11.83	$50.4 \pm 13.2$
10	Water	$9.75 \pm 1.04$	$10.06 \pm 0.77$	2.53	-0.65	$21.9 \pm 7.9$
5.96	Air	$5.35 \pm 0.91$	$6.37 \pm 1.07$	10.18	-6.92	$17.9 \pm 6.7$
5.96	Water	$5.54 \pm 0.77$	$6.44 \pm 0.88$	7.09	-7.97	$16.8 \pm 10.0$

ations correspond to the arrangement of actin and myosin filaments, which are crucial for the contractile function of smooth muscle cells. The higher apparent thickness values are concentrated around the center, highlighting the distinction between the nucleus and cytoplasmic regions. The monocyte images (panels g-i) show a highly pronounced phase shift and substantial thickness, exceeding 15  $\mu\text{m}$ , reflecting the complex morphology of the cell. The phase variations captured in this image provide insight into the internal complexity of the monocyte, which is essential for studying its role in the immune response and its interactions with pathogens. Taken together, these findings demonstrate the utility of TIE-based phase retrieval for qualitative visualization and apparent thickness estimation in cellular samples.

To characterize the computational overhead associated with TIE-based phase imaging under electronic defocus, the processing time of individual pipeline components was measured on the Jetson Orin NX platform.

Specifically, the execution times of ETL-based defocus settling, three-plane image acquisition, FFT-based TIE phase reconstruction, and YOLOv8-based instance segmentation were profiled independently. The electrowetting liquid lens exhibited a mean settling time of  $24.56 \pm 1.47$  ms per defocus step (Supplementary Fig. S6). Three-plane image acquisition, including electronic defocus actuation and software-triggered capture, required  $82 \pm 12$  ms per TIE stack when measured at the Python control layer. TIE phase reconstruction required  $28 \pm 3$  ms

per stack when applied to cropped single-cell regions of interest. For completeness, full-frame TIE reconstruction over the entire sensor area ( $3840 \times 2160$  pixels) required approximately 4.6 s per stack on the Jetson Orin NX.

These measurements quantify the relative computational cost associated with phase reconstruction. During routine operation, image acquisition and AI inference are executed asynchronously. In the present experiment, single-cell regions of interest were manually cropped; however, in future implementations this step can be fully automated by extracting bounding boxes from YOLOv8 detections. Accordingly, TIE-based phase imaging is employed primarily for quantitative visualization and offline validation rather than for continuous real-time processing, while low-latency segmentation and tracking are performed exclusively on in-focus bright-field images.

### 3.3. Edge computing powered instance segmentation and counting

Numerous compact microscopy systems have been developed as standalone imaging platforms that require external computational resources for image processing, storage, and analysis [6,50,51]. Although such configurations facilitate deployment in challenging environments, such as high-humidity cell incubators, the reliance on external computing infrastructure renders these systems cumbersome and less portable. Furthermore, the absence of integrated advanced analytical capabili-

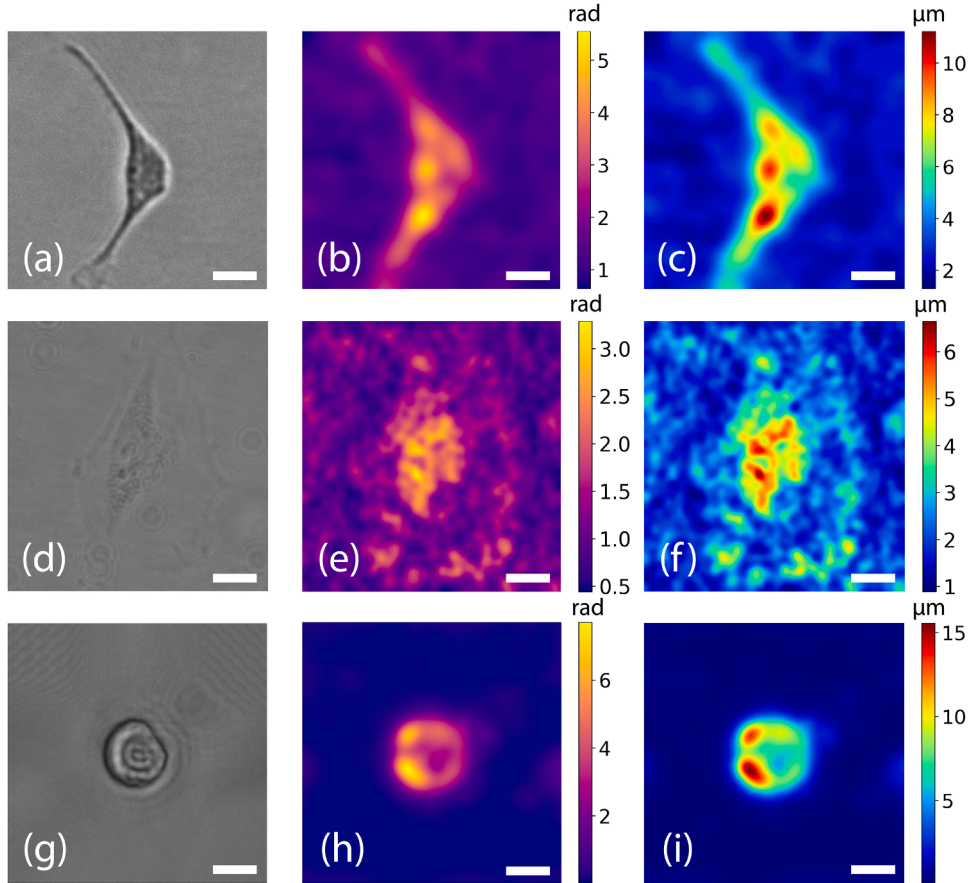


**Fig. 5.** The original in-focus images are (a), (d), and (g), the TIE phase retrieved images in radian are (b), (e), and (h) and the apparent thicknesses under assumed RI<sub>s</sub> image in  $\mu\text{m}$  is (c), (f), and (i) of an endothelial cell, a smooth muscle cell, and a monocyte respectively at a defocus distance of 12  $\mu\text{m}$ . Scale bars denote 5  $\mu\text{m}$ .

ties in these designs limits the ability of researchers to make immediate data-driven decisions during experiments. To address these limitations, the proposed microscope integrates edge computing with deep learning algorithms, enabling on-device processing and low-latency analysis, thereby enhancing operational efficiency and portability.

For automated image analysis, this study used YOLOv8 convolutional neural network, renowned for its efficacy in real-time object detection and segmentation [41]. The YOLOv8 architecture, featuring an anchor-free CSPDarknet53 backbone with Cross Stage Partial (CSP) connections, a Path Aggregation Network (PANet) neck, and a dynamic anchor assignment head, was utilized to perform both single-class and multiclass instance segmentation of cellular images (Supplementary Figure S13). The model was initialized with pre-trained YOLOv8m weights and fine-tuned on a dataset comprising 150 images, equally distributed across three cell types: bEnd.3, A-10, and THP-1. Training was conducted over 250 epochs on the NVIDIA Jetson Orin NX, with a learning rate of 0.002 and momentum of 0.9, achieving a confidence threshold of 0.8 for segmentation inference.

Segmentation effectiveness was assessed with the mean averaged precision (mAP) metric at an intersection over union (IoU) threshold of 0.5. The mAP values for single-class segmentation were 74.0% for bEnd.3, 86.7% for A-10, and 88.3% for THP-1, demonstrating consistent detection performance across diverse cellular morphologies. Multiclass segmentation of all three cell types yielded an mAP of 75.4%, underscoring the ability of the model to accurately delineate multiple cell types within a co-culture system. The inference time for multiclass segmentation averaged  $153.58 \pm 20.28$  ms per frame across 50 images, enabling low-latency processing. Automated cell counting was seamlessly integrated into the segmentation pipeline, with results visualized in Sup-

plementary Figure S15 (a-f) for single-class segmentation and Fig. 6 for multiclass segmentation with bounding boxes. The sensitivity of the model to varying cell shapes and sizes, without reliance on staining techniques, highlights its utility in label-free biomedical imaging and its potential for estimating cell confluence in dynamic culture systems.

To assess the computational efficiency of edge-based processing, the YOLOv8 multiclass segmentation model was trained on both the NVIDIA Jetson Orin NX (edge device) and the NVIDIA RTX 3080 Ti (high-performance computing system) using the same 150-image dataset. Training on the Jetson Orin achieved a segmentation loss of 1.0987 after 160 epochs, compared to 1.1234 for the RTX 3080 Ti. Similarly, the mAP reached 0.8052 on the Jetson Orin and 0.8033 on the RTX 3080 Ti after 167 epochs. Despite comparable performance in segmentation loss and mAP, the Jetson Orin required significantly longer training time (2.52 hours) compared to the RTX 3080 Ti (0.260 hours), reflecting the trade-off between computational power and portability. The Jetson Orin exhibited a faster initial reduction in segmentation loss and slightly higher mAP consistency, as illustrated in Supplementary Figure S14 (a-b). These results underscore the feasibility of deploying sophisticated deep learning models on resource-constrained edge devices, which facilitates portable microscopy applications in diverse settings.

The validation of the multiclass segmentation model was further corroborated through live-cell assays, where endothelial cells stained with Calcein AM fluoresced green, while smooth muscle cells remained unstained, allowing clear differentiation. The distinct segmentation masks for endothelial and smooth muscle cells, as shown in Fig. 6d, affirm the precision of the YOLOv8 model in resolving complex cellular populations. This capability enhances the applicability of the system in

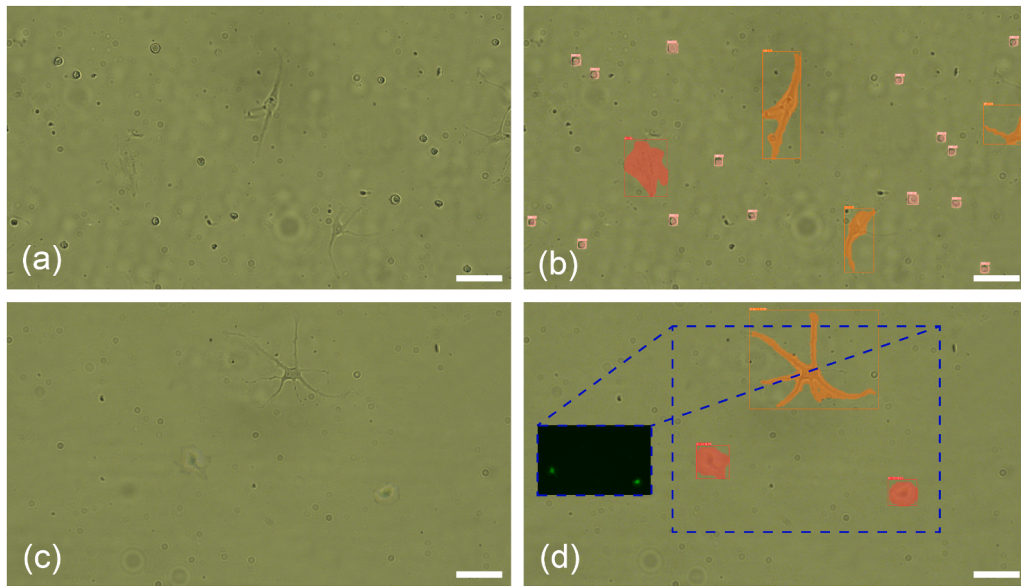


**Fig. 6.** Multi-class instance segmentation of endothelial cells, smooth muscle cells, and monocytes is depicted in (a) and (b). Validation of multi-class segmentation for endothelial cells and smooth muscle cells using a live cell assay is presented as an inset in (d) with endothelial cells labeled with calcein-AM green fluorescence. Scale bars denote 20  $\mu\text{m}$ .

studying cellular interactions and dynamics without the need for invasive labeling techniques.

#### 3.4. Tracking of segmented cells

To elucidate the dynamic behavior of cellular populations, the TrackPy library was used to track bEnd.3 endothelial cells and THP-1 monocytes following instance segmentation with the YOLOv8 convolutional neural network. TrackPy [48], a Python-based framework for particle tracking, leveraged the centroid coordinates extracted from YOLOv8 segmentation results to reconstruct spatiotemporal cell trajectories with reasonable spatial accuracy.

Analysis revealed distinct migratory behaviors between cell types. Monocytes exhibited directed motility with a mean velocity of 2.91  $\mu\text{m}/\text{s}$ , whereas endothelial cells displayed slower random movement with an average speed of 0.22  $\mu\text{m}/\text{s}$ . These observed velocities align with the expected biological characteristics of immune and endothelial cells in culture.

Continuous tracking was achieved with consistency over extended observation periods. Approximately 85% of endothelial cells were successfully tracked for up to 30 hours, while 91% of monocytes were tracked over 2 minutes, reflecting the different temporal scales of their migration behaviors. Cell trajectories were linked using TrackPy with a search range of 15 pixels (corresponding to observed velocities of 1–2  $\mu\text{m}/\text{s}$ ), a memory of 5 frames to tolerate transient detection losses, and an adaptive stop threshold of 5 pixels.

Tracking performance was quantitatively evaluated against manually annotated ground-truth trajectories using metrics from the CLEAR MOT framework [49]. Spatial localization fidelity was assessed using Multiple Object Tracking Precision (MOTP), yielding a value of 82% in triplicate datasets, corresponding to a mean Euclidean positional deviation of less than 5% of the average cell diameter (5–10  $\mu\text{m}$ ) over the recorded periods. In addition, configuration-level tracking robustness was assessed using Multiple Object Tracking Accuracy (MOTA), which accounts for missed detections, false positives, and identity mismatches. The measured average MOTA values were  $72.95 \pm 0.23\%$  across triplicate data.

Cells that entered or exited the field of view, underwent mitosis, or produced incomplete trajectories due to boundary effects were excluded from evaluation to avoid bias from non-trackable biological events,

consistent with established practices in biological cell-tracking benchmarks [40]. Representative cell trajectories are visualized in time-lapse format in Supplementary Movie S1 and Movie S2.

#### 4. Discussion

This work presents a compact, liquid-lens-based benchtop microscope that integrates TIE-based phase imaging and edge AI analysis within a portable, 3D-printed platform. The system is housed in a polyamide chassis fabricated via selective laser sintering, with an emphasis on mechanical stability, compact form factor, and compatibility with live-cell imaging environments. An electrowetting liquid lens enables rapid, vibration-free axial focusing with limited magnification variation ( $3.3 \pm 0.2\%$  over a 5.9 mm range), providing a practical approach for acquiring the defocused intensity images required for TIE phase reconstruction without mechanical translation or interferometric optical components.

The performance of TIE-based phase reconstruction was evaluated using polystyrene microspheres with nominal diameters of 5  $\mu\text{m}$  and 10  $\mu\text{m}$  as calibration objects, enabling direct assessment of phase recovery and phase-to-apparent-thickness conversion under known refractive index conditions. Additional verification was conducted using fluorescent reference beads with a mean diameter of 5.96  $\mu\text{m}$  to examine consistency across bead types and imaging modalities. For the 10  $\mu\text{m}$  microspheres, apparent thickness deviations as low as 2.53% were observed in aqueous media, indicating stable and repeatable phase reconstruction for objects with well-defined geometry and refractive index. Smaller beads exhibited larger relative deviations, consistent with increased sensitivity to refractive index uncertainty, signal-to-noise limitations, and partial coherence effects. These results demonstrate that ETL-based TIE reconstruction can be reliably implemented in a compact, relay-free microscope for calibration objects and for qualitative-to-semi-quantitative phase visualization.

For biological cells, reconstructed phase and apparent thickness maps provide label-free visualization of cellular morphology and optical path length variations. Because cellular refractive indices are not precisely known and may vary spatially and temporally, retrieved thickness values should be interpreted as apparent thickness under assumed refractive index contrast rather than as absolute physical thickness. Nevertheless, the phase reconstructions consistently reveal relative

morphological features, internal optical heterogeneity, and cell-to-cell variations, supporting their use for qualitative interpretation and comparative analysis across experimental conditions.

In the current system architecture, phase reconstruction and AI-based image analysis are implemented as parallel and functionally decoupled modules. TIE-based phase imaging is primarily employed for quantitative visualization, system validation, and offline analysis, whereas automated segmentation and tracking are performed exclusively on in-focus bright-field images to ensure low-latency performance on edge hardware. This modular design avoids direct dependence of AI inference on phase reconstruction quality and enhances robustness under varying illumination and sample conditions.

Although phase reconstruction is presently executed independently of the AI pipeline, the modular architecture permits future integration in a selective and latency-aware manner. Specifically, bounding boxes generated by the YOLOv8 detector could be used to automatically crop regions of interest containing individual cells, which may then be processed through TIE-based phase reconstruction on demand. By restricting phase computation to localized regions rather than full-frame images, such an approach could enable low-latency phase analysis for selected targets without compromising real-time segmentation and tracking performance.

Automated instance segmentation and cell counting were implemented using a YOLOv8 model deployed on an NVIDIA Jetson Orin NX edge device, achieving mAP values of 74.0%, 86.7%, and 88.3% for endothelial cells, smooth muscle cells, and monocytes, respectively, and 75.4% for multiclass segmentation at an IoU threshold of 0.5. These results demonstrate that accurate bright-field-based segmentation and tracking can be performed on-device with low latency, without reliance on external computing resources. In addition, integration of an ITO-based transparent heater with closed-loop temperature control enables stable live-cell imaging over extended periods, supporting time-lapse experiments under physiologically relevant conditions.

Overall, the system presents a practical implementation of a compact microscope that integrates non-interferometric phase reconstruction with on-device AI analysis in a modular architecture. Rather than aiming to replace interferometric or laboratory-grade quantitative phase microscopes, the proposed platform is intended to complement existing systems by enabling portable, label-free phase visualization and automated analysis in space- or resource-constrained environments.

## 5. Conclusion

In this work, we presented a compact AI-enabled microscope that combines electronically tunable optics, non-interferometric phase reconstruction, and on-device deep learning within a portable platform. The system enables label-free phase visualization and morphological assessment while supporting low-latency bright-field-based segmentation and tracking on edge hardware.

By adopting a modular architecture that decouples phase reconstruction from real-time AI inference, the platform achieves robust operation with a clearly defined quantitative scope and flexibility for future extensions. The proposed system is intended to complement existing imaging tools by providing portable, automated, and label-free imaging capabilities for biophotonics and AI-driven biomedical applications.

## Declaration of generative AI and AI-assisted technologies in the manuscript preparation process

During the preparation of this work, the authors used GPT5.2 to assist with grammar and language refinement. After using this service, the authors reviewed and edited the content as necessary and take full responsibility for the final version of the published article.

## CRediT authorship contribution statement

**Hsieh-Fu Tsai:** Writing – review & editing, Writing – original draft, Supervision, Software, Methodology, Investigation, Funding acquisition, Conceptualization; **Soumyajit Podder:** Writing – original draft, Visualization, Software, Methodology, Investigation, Formal analysis, Data curation; **I-Ming Chang:** Writing – original draft, Visualization, Software, Methodology, Investigation, Formal analysis, Data curation; **Mao-Chang Ho:** Investigation, Data curation.

## Data availability

The data underlying the results presented in this paper are available upon request.

## Disclosures

A patent has been filed for the edge AI QPI microscope described in this paper (Case No. 114142794, Intellectual Property Office, Ministry of Economic Affairs, Republic of China Taiwan), with H.-F. Tsai and S. Podder listed as inventors.

## Funding

Individual grants funded this work to H.-F. T. from the Okinawa Institute of Science and Technology Graduate University Technology Pioneer Fellowship, National Science and Technology Council, Taiwan, and Chang Gung Memorial Hospital, Taiwan (NSTC112-2221-E-182-012-MY3 and CMRPD1N0351). We thank NVIDIA Corporation for hardware support through the NVIDIA Applied Research Accelerator Program awarded to H.-F. T. The funders had no role in study design, data collection and analysis, decision to publish, or preparation of the manuscript.

## Supplemental document

See Supplementary Document 1 for supporting content. The Supplementary Movies S1 and S2 are publicly accessible on the Zenodo repository at <https://doi.org/10.5281/zenodo.16731392>.

## Declaration of competing interests

The authors declare the following financial interests/personal relationships which may be considered as potential competing interests:

Hsieh-Fu Tsai reports financial support was provided by National Science and Technology Council. Hsieh-Fu Tsai reports financial support was provided by Chang Gung Memorial Hospital Linkou Branch. Hsieh-Fu Tsai reports equipment, drugs, or supplies was provided by NVIDIA Corporation. Hsieh-Fu Tsai has patent #114142794 pending to Chang Gung University. If there are other authors, they declare that they have no known competing financial interests or personal relationships that could have appeared to influence the work reported in this paper.

## Acknowledgments

The authors thank Mr. Kazumi Toda-Peters and Prof. Amy Q. Shen at [Okinawa Institute of Science and Technology Graduate University](#) for their assistance in fabricating the staircase thickness reticle. The authors thank Prof. Ji-Yen Cheng at the Research Center for Applied Sciences, [Academia Sinica](#), Taiwan, for technical assistance. The authors thank the [Chang Gung University](#) Microscopy Center for technical assistance.

## Supplementary material

Supplementary material associated with this article can be found in the online version at [10.1016/j.optlaseng.2026.109659](https://doi.org/10.1016/j.optlaseng.2026.109659).

## References

- [1] Diederich B, Lachmann R, Carlstedt S, Marsikova B, Wang H, Uwurukundo X, et al. A versatile and customizable low-cost 3d-printed open standard for microscopic imaging. *Nat Commun* 2020;11(1):5979.
- [2] Zehrer AC, Martin-Villalba A, Diederich B, Ewers H. An open-source, high-resolution, automated fluorescence microscope. *Elife* 2024;12:RP89826. <https://doi.org/10.7554/eLife.89826>
- [3] Vos BE, Blesa EB, Betz T. Designing a high-resolution, LEGO-based microscope for an educational setting. *The Biophysicist* 2021;2(3):29–40.
- [4] Ghosh KK, Burns LD, Cocker ED, Nimmerjahn A, Ziv Y, Gamal AE, et al. Miniaturized integration of a fluorescence microscope. *Nat Methods* 2011;8(10):871–8.
- [5] Cybulski JS, Clements J, Prakash M, Foldscope: origami-based paper microscope. *PLoS ONE* 2014;9(6):1–11. <https://doi.org/10.1371/journal.pone.0098781>
- [6] Zhang YS, Ribas JA, Nadhman A, Aleman J, Selimović v, Lesher-Perez SC, et al. A cost-effective fluorescence mini-microscope for biomedical applications. *Lab Chip* 2015;15:3661–9. <https://doi.org/10.1039/C5LC00666J>
- [7] Sanz M, Picazo-Bueno JA, Granero L, García J, Micó V. Compact, cost-effective and field-portable microscope prototype based on MISHELF microscopy. *Sci Rep* 2017;7(1):43291.
- [8] Sharkey JP, Foo D CW, Kabla A, Baumberg JJ, Bowman RW. A one-piece 3d printed flexure translation stage for open-source microscopy. *Rev Sci Instrum* 2016;87(2). <https://doi.org/10.1063/1.4941068>
- [9] Knapper J, Whiteford F, Rosen D, Wadsworth W, Stirling J, Mkindi C, et al. Developing the openflexure microscope towards medical use: technical and social challenges of developing globally accessible hardware for healthcare. *Philos Trans R Soc A: Math Phys Eng Sci* 2024;382(2274). <https://doi.org/10.1098/rsta.2023.0257>
- [10] Graham R. A variable focus lens and its uses. *J Opt Soc Am* 1940;30(11):560–3. <https://doi.org/10.1364/JOSA.30.000560>
- [11] Chen L, Ghilardi M, Busfield J JC, Carpi F. Electrically tunable lenses: a review. *Front Robot AI* 2021;8. <https://doi.org/10.3389/frobt.2021.678046>
- [12] Kuiper S, Hendriks BHW. Variable-focus liquid lens for miniature cameras. *Appl Phys Lett* 2004;85(7):1128–30. <https://doi.org/10.1063/1.1779954>
- [13] Mishra K, Van den Ende D, Mugele F. Recent developments in optofluidic lens technology. *Micromachines (Basel)* 2016;7(6). <https://doi.org/10.3390/mi7060102>
- [14] Zhao P, Li Y, Zappe H. Accelerated electrowetting-based tunable fluidic lenses. *Opt Express* 2021;29(10):15733–46. <https://doi.org/10.1364/OE.423460>
- [15] Ren H, Wu S-T. Adaptive liquid crystal lens with large focal length tunability. *Opt Express* 2006;14(23):11292–8. <https://doi.org/10.1364/OE.14.011292>
- [16] Efsthathiou C, Draviam VM. Electrically tunable lenses – eliminating mechanical axial movements during high-speed 3D live imaging. *J Cell Sci* 2021;134(16):jcs258650. <https://doi.org/10.1242/jcs.258650>
- [17] Zernike F. How i discovered phase contrast. *Science* 1955;121(3141):345–9. <https://doi.org/10.1126/science.121.3141.345>
- [18] Pluta M. Nomarski's DIC microscopy: a review. In: Pluta M, Szyjer M, editors. Phase contrast and differential interference contrast imaging techniques and applications; vol. 1846. International Society for Optics and Photonics; SPIE; 1994, p. 10–25. <https://doi.org/10.1117/12.171873>
- [19] Hu C, Popescu G. Quantitative Phase Imaging: Principles and Applications. Cham: Springer International Publishing. ISBN 978-3-030-21722-8; 2019, p. 1–24. [https://doi.org/10.1007/978-3-030-21722-8\\_1](https://doi.org/10.1007/978-3-030-21722-8_1)
- [20] Park Y, Depersinge C, Popescu G. Quantitative phase imaging in biomedicine. *Nat Photon* 2018;12(10):578–89.
- [21] Teague MR. Deterministic phase retrieval: a green's function solution. *J Opt Soc Am* 1983;73(1):1434–41. <https://doi.org/10.1364/JOSA.73.0001434>
- [22] Zuo C, Li J, Sun J, Fan Y, Zhang J, Lu L, et al. Transport of intensity equation: a tutorial. *Opt Lasers Eng* 2020;135:106187. <https://doi.org/10.1016/j.optlaseng.2020.106187>
- [23] Zuo C, Sun J, Li J, Zhang J, Asundi A, Chen Q. High-resolution transport-of-intensity quantitative phase microscopy with annular illumination. *Sci Rep* 2017;7(1):7654.
- [24] Yu W, Tian X, He X, Song X, Xue L, Liu C, et al. Real time quantitative phase microscopy based on single-shot transport of intensity equation (ssTIE) method. *Appl Phys Lett* 2016;109(7).
- [25] Zhang J, Chen Q, Sun J, Tian L, Zuo C. On a universal solution to the transport-of-intensity equation. *Opt Lett* 2020;45(13):3649–52. <https://doi.org/10.1364/OL.391823>
- [26] Grant SD, Richford K, Burdett HL, McKee D, Patton BR. Low-cost, open-access quantitative phase imaging of algal cells using the transport of intensity equation. *R Soc Open Sci* 2020;7(1):191921. <https://doi.org/10.1098/rsos.191921>
- [27] Wang K, Di J, Li Y, Ren Z, Kemao Q, Zhao J. Transport of intensity equation from a single intensity image via deep learning. *Opt Lasers Eng* 2020;134:106233. <https://doi.org/10.1016/j.optlaseng.2020.106233>
- [28] Carvalho G, Cabral B, Pereira V, Bernardino J. Edge computing: current trends, research challenges and future directions. *Computing* 2021;103(5):993–1023.
- [29] Fan Y, Li J, Lu L, Sun J, Hu Y, Zhang J, et al. Smart computational light microscopes (SCLMs) of smart computational imaging laboratory (SCILab). *Photonix* 2021;2:1–64.
- [30] Flórez SL, González-Briones A, Hernández G, Ramos C, de la Prieta F. Automatic cell counting with YOLOv5: a fluorescence microscopy approach. *Int J Interact Multi-media Artif Intell* 2023;8(3):64–71. <https://doi.org/10.9781/ijimai.2023.08.001>
- [31] Grewen BF, Voigt FF, Hoff M vt, Helmchen F. Fast two-layer two-photon imaging of neuronal cell populations using an electrically tunable lens. *Biomed Opt Express* 2011;2(7):2035–46. <https://doi.org/10.1364/BOE.2.002035>
- [32] Jabbour JM, Malih BH, Olsovsky C, Cuenca R, Cheng S, Jo JA, et al. Optical axial scanning in confocal microscopy using an electrically tunable lens. *Biomed Opt Express* 2014;5(2):645–52. <https://doi.org/10.1364/BOE.5.000645>
- [33] Qu Y, Hu Y. Analysis of axial scanning range and magnification variation in wide-field microscope for measurement using an electrically tunable lens. *Microsc Res Tech* 2019;82(2):101–13. <https://doi.org/10.1002/jemt.23113>
- [34] Tsai H-FT, MAX14574 I2C Python library (jul. 2024). <https://doi.org/10.5281/zendo.12788338>
- [35] Li J, Chen Q, Zhang J, Zhang Y, Lu L, Zuo C. Efficient quantitative phase microscopy using programmable annular LED illumination. *Biomed Opt Express* 2017;8(10):4687–705. <https://doi.org/10.1364/BOE.8.0004687>
- [36] Koren N. The imatest program: comparing cameras with different amounts of sharpening. In: Sampat N, DiCarlo JM, Martin RA, editors. Digital photography II; vol. 6069. International Society for Optics and Photonics; SPIE; 2006, p. 60690L. <https://doi.org/10.1117/12.650848>
- [37] Schindelin J, Arganda-Carreras I, Frise E, Kaynig V, Longair M, Pietzsch T, et al. Fiji: an open-source platform for biological-image analysis. *Nat Methods* 2012;9(7):676–82. <https://doi.org/10.1038/nmeth.2019>
- [38] Ronneberger O, Fischer P, Brox T. U-Net: convolutional networks for biomedical image segmentation. In: Navab N, Hornegger J, Wells WM, Frangi AF, editors. Medical image computing and computer-Assisted intervention – MICCAI 2015. Cham: Springer International Publishing. ISBN 978-3-319-24574-4; 2015, p. 234–41.
- [39] Bove A, Gradić D, Fujita Y, Banerjee S, Charras G, Lowe AR. Local cellular neighborhood controls proliferation in cell competition. *Mol Biol Cell* 2017;28(23):3215–28. PMID: 28931601. <https://doi.org/10.1091/mbc.e17-06-0368>
- [40] Tsai H-F, Gajda J, Sloan T FW, Rares A, Shen AQ, Usiagaci: instance-aware cell tracking in stain-free phase contrast microscopy enabled by machine learning. *SoftwareX* 2019;9:230–7. <https://doi.org/10.1016/j.softx.2019.02.007>
- [41] Jocher G, Chaurasia A, Qiu J. Ultralytics YOLO (jan. 2023). 2023. <https://github.com/ultralytics/ultralytics>
- [42] Guigay JP, Langer M, Boistel R, Cloetens P. Mixed transfer function and transport of intensity approach for phase retrieval in the fresnel region. *Opt Lett* 2007;32(12):1617–19. <https://doi.org/10.1364/OL.32.000167>
- [43] Gureyev TE, Nugent KA. Phase retrieval with the transport-of-intensity equation. II: orthogonal series solution for nonuniform illumination. *J Opt Soc Am A* 1996;13(8):1670–82. <https://doi.org/10.1364/JOSAA.13.001670>
- [44] Zuo C, Chen Q, Qu W, Asundi A. High-speed transport-of-intensity phase microscopy with an electrically tunable lens. *Opt Express* 2013;21(20):24060–75. <https://doi.org/10.1364/OE.21.024060>
- [45] Patel S, Tutchenko L. The refractive index of the human cornea: a review. *Contact Lens Anterior Eye* 2019;42(5):575–80. <https://doi.org/10.1016/j.clae.2019.04.018>
- [46] Curl CL, Bellair CJ, Harris T, Allman BE, Harris PJ, Stewart AG, et al. Refractive index measurement in viable cells using quantitative phase-amplitude microscopy and confocal microscopy. *Cytometry Part A* 2005;65A(1):88–92. <https://doi.org/10.1002/cyto.a.20134>
- [47] Dannhauser D, Rossi D, Ripaldi M, Netti PA, Causa F. Single-cell screening of multiple biophysical properties in leukemia diagnosis from peripheral blood by pure light scattering. *Sci Rep* 2017;7(1). <https://doi.org/10.1038/s41598-017-12990-4>
- [48] Allan DB, Keim NC, Caswell TA, van der Wel CM, Trackpy: fast, flexible particle tracking toolkit. 2014. <https://soft-matter.github.io/trackpy/v0.6.4/>
- [49] Bernardin K, Stiefelhagen R. Evaluating multiple object tracking performance: the CLEAR MOT metrics. *EURASIP J Image Video Process* 2008;2008:1–10. <https://doi.org/10.1155/2008/246309>
- [50] Kahle J, Levin R, Niles W, Rasnow B, Schelein M, Shumate C. An inexpensive simple-to-use inverted fluorescence microscope: a new tool for cellular analysis. *JALA: J Assoc Lab Automat* 2010;15(5):355–61. <https://doi.org/10.1016/j.jala.2010.06.008>
- [51] Serioli L, Gruzinckyte L, Zappalá G, Hwu ET, Laksafoss TZ, Jensen PL, et al. Moving perfusion culture and live-cell imaging from lab to disc: proof of concept toxicity assay with AI-based image analysis. *Lab Chip* 2023;23:1603–12. <https://doi.org/10.1039/D2LC00984F>